Femtosecond laser ablation of nickel in vacuum

S Amoruso[1], R Bruzzese[1,3], X Wang[1], N N Nedialkov[2] and P A Atanasov[2]

[1] Coherentia CNR-INFM and Dipartimento di Scienze Fisiche, Università degli Studi di Napoli Federico II, Complesso Universitario di Monte S. Angelo, Via Cintia, I-80126 Napoli, Italy
[2] Institute of Electronics, Bulgarian Academy of Sciences, 72 Tsaridradsko shose Boulevard, Sofia 1784, Bulgaria

E-mail: bruzzese@na.infn.it

Abstract
We present an experimental characterization and a theoretical analysis of ultrashort laser ablation of a nickel target, which highlights the more general and peculiar features of femtosecond (fs) laser ablation of metals. The study has been carried out by using visible (527 nm) laser pulses of ≈ 300 fs duration. The vacuum expansion dynamics of the ablated species has been investigated by using fast photography and optical emission spectroscopy, while the fs laser pulse–metal interaction has been studied theoretically by means of molecular dynamics simulations. Special attention has been given to the study of the dependence of ablation depth on laser fluence, which has been carried out by comparing the SEM analysis of micro-holes drilled into the nickel samples with the predictions of the theoretical model. The main outcomes of our investigation, which are very satisfactorily reproduced and accounted for by the theoretical model, are (i) the nonlinear dependence of the ablation yield on the laser fluence, and its reliance to the electron heat diffusion, in the process of redistribution of the absorbed energy, (ii) the splitting of the material blow-off into two main classes of species, atoms and nanoparticles, characterized by different expansion dynamics, and (iii) the different degrees of heating induced by the laser pulse at different depths into the material, which causes the simultaneous occurrence of various ablation mechanisms, eventually leading to atoms and nanoparticles ejection.

1. Introduction

The interaction of intense, sub-picosecond laser pulses with solid targets has generated a lot of interest in recent years due to the variety of possibilities offered both in basic science and for technological applications. The use of femtosecond (fs) laser pulses opens up the opportunity to decouple the initial photo-excitation of the target material from the subsequent dynamics of the removed material, contrary to what happens with pulses of longer temporal duration. Lasers with fs pulse duration are of particular interest for ablation as the pulse width is less than the typical electron-lattice thermalization time, which is of the order of a few picoseconds. This feature allows to drive the irradiated material into an extremely excited state followed by a rapid quenching, which finally results in a material blow-off composed of fast ions and atoms as well as clusters and nanoaggregates of the target material, depending on the processing parameters [1, 2]. Recently, laser ablation with fs laser pulses has also been recognized as an interesting technique for the generation of nanoparticles (NPs) of metals and semiconductors [3, 4], as well as for the deposition of nanoparticle films with peculiar physical properties [5].

Despite the demonstration of the potentiality of ultrashort laser pulses in different contexts (e.g. micromachining, film deposition, NPs production, etc) the fundamental mechanisms of importance in laser–matter interaction, and following material relaxation, as well as the resulting plume structure and

---

[3] Author to whom any correspondence should be addressed.

expansion dynamics, are still under discussion. Therefore, in addition to the experimental work, numerous theoretical and numerical studies aiming to elucidate the intrinsic mechanisms of ultrashort laser–matter interaction have been undertaken. A large part of these studies are based on the well-known two-temperature model (TTM) [6], which describes the energy exchange between the electrons and lattice subsystems (assumed to be in thermodynamic equilibrium at different temperatures) during the characteristic relaxation time of the material. Hydrodynamic modelling and molecular dynamics (MD) simulations were also considered by different authors to describe the features of ultrashort laser ablation and the subsequent plasma plume formation [4, 7–10]. The several investigations provide a richness of information about ultrashort laser interaction with solids and demonstrate the complexity involved in the process, which critically depends on both the processing conditions and the material properties. This claims for specific experimental and numerical studies of selected systems in well-defined conditions.

In this context, the present work deals with an experimental investigation and theoretical modelling of the laser ablation of a nickel target with 527 nm, $\approx$300 fs laser pulses in high vacuum conditions. In particular, the regime of ablation pertaining to a range of fluences going from the threshold ($\approx$0.1 J cm^{-2}) up to the level of very efficient ejection of material ($\approx$1 J cm^{-2}) is considered. This range is of particular interest in material processing, NPs generation and thin films deposition. The main aim of this study is to single out and clarify the principal features characterizing the process. To this end we use time-gated optical imaging and optical emission spectroscopy to characterize the plume structure and expansion dynamics in vacuum. The experimental analysis evidences the splitting of the ejected species in two main components: (a) a first cloud of fast atomic species, which leaves the target surface with rather high expansion velocities of the order of a few tens of km s^{-1}; (b) a secondary plume component constituted of Ni NPs expanding in vacuum with flight velocities of more than ten times smaller than the velocity characterizing the atomic component. This second cloud is characterized by a quite different expansion dynamics, remaining close to the target surface for a very long time after the laser pulse onset. In parallel, we have also studied theoretically fs ablation of Ni by MD simulations with the aim of supporting and interpreting the experimental observations. The MD technique actually provides a detailed atomic-level picture of the emission of the particles, clearly confirming that the formation of two classes of species, atoms and nanoclusters is a prominent and very specific feature of matter removal from the metal targets by fs laser irradiation in vacuum. In particular, this feature can be associated with the different heating conditions produced by the ultrashort laser pulse into the material at various distances from the target surface, which results in the simultaneous presence of different ablation mechanisms at different depths into the solid [7–9].

We have also carried out a thorough analysis of the laser fluence dependence of the ablation process in the range which is of concern here, i.e. $\approx$0.1–1 J cm^{-2}. In particular, we have compared the experimental dependences of the ablation depth with the ablation rate obtained by the MD calculations, obtaining a fairly good agreement. The observed nonlinear dependence of the ablation yield with the laser fluence is, finally, associated with the contribution of the electron heat diffusion in the process of redistribution of the absorbed energy.

The paper is organized in five sections. A description of the experimental setup and procedure is given in section 2, while the MD model is presented in section 3. The experimental results and the predictions of the MD simulations are compared and discussed in section 4. Finally, the summary and conclusions are reported in section 5.

2. Experimental

The experimental apparatus is very similar to that used in our previous works on ultrashort laser ablation of different targets [11]. The laser pulses are provided by a Nd : Glass laser system delivering $\approx$300 fs pulses at 527 nm obtained by the second-harmonic-generation pulse compression of the fundamental output (i.e. 1055 nm, $\approx$0.9 ps). The temporal profile of the laser pulse has been monitored by a single-shot background-free autocorrelation technique. The emitted energy per pulse is of the order of $\approx$1.3 mJ at 527 nm at a typical repetition rate of 33 Hz. During the experiments the repetition rate has been changed by means of a mechanical shutter. The laser pulse energy could be varied by means of calibrated attenuating plates. The metal target is placed in a vacuum chamber evacuated to a residual pressure of $\leqslant 10^{-7}$ mbar.

Micro-hole drilling experiments were carried out in high vacuum by focusing the laser radiation on the Ni (99.99%) samples surface, at normal incidence. Scanning electron microscopy (SEM) analysis has been used to obtain the total depth of holes drilled into the samples at different laser fluences. The ablation rate (depth per pulse) has been obtained as the total depth produced by a given number of laser pulses divided by the number of laser shots. In all the cases the aspect ratio of the holes (i.e. depth to diameter ratio) was below 1, thus minimizing any effect of deep-hole confinement on the results obtained by averaging the ablation rate.

The vacuum expansion dynamics of the ablated species has been studied by fast photography and optical emission spectroscopy. In these experiments the laser beam hits the target at an incident angle of 45°, and in *p*-polarization, thus allowing also the collection of the ablation plume on a suitable substrate located in front of the target surface [11].

Different viewing ports of the vacuum chamber allow monitoring of the optical emission accompanying the ablation plume along the axes parallel (x) and perpendicular (z) to the target surface. The plume expansion in vacuum has been investigated by acquiring single-shot images of the plume emission, in the x–z plane, with an intensified charge-coupled device camera (ICCD) operating in time-gated detection mode (3 ns minimum temporal resolution). Each image was recorded by imaging the plume total emission onto the ICCD, equipped with a 1024 $\times$ 1024 array, with a 3 : 1 magnification. To reduce the noise, a 2$\times$ binning has been operated during image acquisition obtaining a spatial resolution of $\approx$100 μm. Spectrally resolved measurements of the plume emission have also been carried out by imaging a slice of the plasma onto the entrance of an optical fibre abutted to the entrance slit of a 1/4 m monochromator equipped with two, user selectable,

gratings: a 100 grooves mm^{-1} grating allows the collection of low-resolution spectra in the wavelength range between 250 and 750 nm, while a 1200 grooves mm^{-1} is used for high-resolution analysis of emission in any selected wavelength range. The resulting dispersed emission spectrum is analysed by an ICCD camera, with an overall spectral resolution of ≈ 0.4 nm.

3. The model

The ablation process of Ni is simulated by the classical MD technique [12]. A Morse potential has been used to describe the interaction between the particles, and its specific parameters taken from [13]. Although other potentials based on the more precise embedded atom method (EAM) have been recently developed and applied to metals [14], the choice of the pair Morse potential has been made since it has been proven to give a good description of the interaction between atoms in face-centred-cubic metals, such as nickel, and to predict many material properties. Moreover, the Morse potential was already used by other authors with good agreement between the numerical and the experimental results [7, 15]. In this regard, it is now well established that both the EAM and the Morse potential lead to very similar quantitative descriptions of the process of ultrashort laser ablation of metals [16]. We have, therefore, considered the Morse potential for the present study because its simpler form allows us to use a relatively large number of atoms. This, in turn, permits the use of a larger size of the modelled system and an extension of the simulation time, which are very important for investigating the features of the laser ablation process.

In order to simulate an infinite material in lateral directions, periodic boundary conditions are imposed in the x–y directions. Specific boundary conditions are applied on the bottom of the computational cell in order to prevent the reflection of shock waves [17]. The initial configuration of the modelled material is obtained by arranging $50 \times 3 \times 500$ ($\approx 3 \times 10^5$ Ni atoms) face centred cubic unit cells in the x, y and z direction, respectively, and whose dimensions are $17.6 \times 1.1 \times 176$ nm^3. The simulations start at a temperature of 300 K.

The absorption of laser energy and redistribution of the heat into the metal is governed initially by the free electrons. Since the electrons are not included explicitly in the MD model, their role, and the heating of the material, are taken into account by using the one dimensional two-temperature diffusion model [6]:

$$C_e \frac{\partial T_e}{\partial t} = -\frac{\partial Q_e(z)}{\partial z} - \gamma(T_e - T_i) + S(t), \qquad (1)$$

$$C_i \frac{\partial T_i}{\partial t} = -\frac{\partial Q_i(z)}{\partial z} + \gamma(T_e - T_i), \qquad (2)$$

$$Q_{e(i)}(z) = -k_{e}(i)\frac{\partial T_{e(i)}}{\partial z}, \qquad S(t) = I(t)A\alpha \exp(-\alpha z). \qquad (3)$$

Here, T_e and T_i are the electron and lattice temperatures, respectively, while z is the coordinate perpendicular to the material surface, and $Q(z)$ the heat flux. $S(t)$ and $I(t)$ are the laser energy source and laser intensity distribution

in time, respectively. In particular, the distribution of the incident radiation inside the target, i.e. along the z direction is assumed to follow Beer's law and it is incorporated in the source term $S(t)$. Moreover, we assume a uniform spatial distribution of the incident laser pulse intensity in the x–y directions on the sample surface due to the small dimensions of the simulation system used. In equation (3), $A = (1 - R)$ is the absorbance of a material of reflectivity R and α is the linear absorption coefficient ($\alpha = 7.4 \times 10^{-7}$ m^{-1}) [18], respectively. The optical laser penetration depth (skin depth) is $\ell_{opt} = \alpha^{-1}$. C_e, C_i, k_e and k_i are the heat capacities and thermal conductivities of the electron system and of the lattice, respectively. Finally, the coupling parameter γ describes the rate of energy exchange between the electrons and the lattice.

The values of the parameters for Ni used in the present calculations are taken from the literature: $\gamma = 3.6 \times 10^{17}$ W m^{-3} K^{-1} and $C_i = 4.1 \times 10^6$ J m^{-3} K^{-1} (assumed to be constant) [18, 19]. The reflectivity R of the nickel was considered to be $R = 0.6$ for normal incidence, and $R = 0.51$ for $45°$ incidence and p-polarization. The temperature dependences of the electron heat capacity and the electron heat conductivity are taken according to the following relations [19, 20]:

$$C_e = A_e T_e, \qquad (4)$$

$$K_e = \mu\theta_e \frac{\left(\theta_e^2 + 0.16\right)^{\frac{5}{4}}\left(\theta_e^2 + 0.44\right)}{\left(\theta_e^2 + 0.092\right)^{\frac{1}{2}}\left(\theta_e^2 + \beta\theta_i\right)}, \qquad (5)$$

where $A_e = 1065$ J m^{-3} K^{-2}, $\theta_e = T_e/T_F$ and $\theta_i = T_i/T_F$, where T_F is the Fermi temperature of Ni ($T_F = 1.36 \times 10^5$ K) [21]. The parameters μ and β are estimated to be 229.89 W m^{-1} K^{-1} and 0.17, respectively, as obtained by using the relation $K_e = K_{eo}(T_e/T_i)$, where $K_{eo} = 91$ W m^{-1} K^{-1} [19], which is valid at low electron temperatures [21].

The calculations have been performed for a laser pulse with a wavelength of 527 nm and a duration $\tau_L = 300$ fs (FWHM). The laser intensity has been assumed to have a Gaussian temporal profile, $I(t) = I_0 \exp(-t^2/2\sigma^2)$, where σ is related to τ_L as $\tau_L = \sigma\sqrt{8\ln(2)}$. The laser fluence F is used in the discussion of the results, which is related to the peak intensity I_0 as $F = \sqrt{\pi/4\ln(2)}I_0\tau_L \approx 1.0645I_0\tau_L$. Finally, the ablation process has been investigated in vacuum conditions.

Equations (1)–(3) have been solved using a classical finite difference scheme [22]. In the model presented the material is divided into layers in the z direction. The thickness of each layer is equal to the cut-off radius for the Morse potential used (0.7 nm). The temperature $T_i(z)$ predicted by the two-temperature model is implemented in the MD by a scaling of the atom's velocities in each layer.

4. Results and discussions

4.1. Plume characteristics and vacuum expansion

Figure 1 reports two characteristic ICCD images of the nickel ablation plume in the x–z plane recorded at two different time delays with respect to the arrival of the laser pulse, and at a representative fluence $F \approx 0.8$ J cm^{-2}. Each image is normalized to its maximum intensity and is shown in logarithmic scale. In particular, panels (a) and (b) show
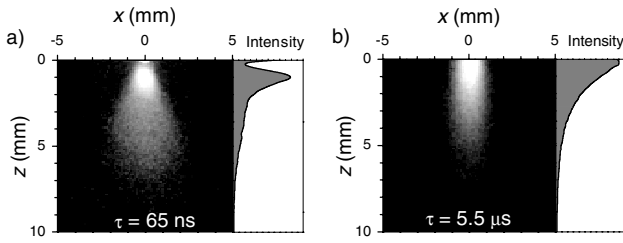
Figure 1. Snapshots of the nickel plume emission at two different time delays τ with respect to the laser pulse onset registered at a laser fluence $F \approx 0.8\,\mathrm{J\,cm^{-2}}$: (*a*) short time delays—emission from the atomic plume component; (*b*) long time delays—emission from the nanoparticles plume component (see text for details). In the images $z = 0$ mm defines the front face of the target.

snapshots of the plume emission acquired at time delays τ of 65 ns and 5.5 μs after the laser pulse onset, respectively. The two images of figure 1 are representative of the plume images at short (<500 ns) and long ($>1\,\mu$s) temporal delays after the laser pulse. From the snapshots of figure 1 we observe that the plume is fairly symmetric about the surface normal, and we can also ascertain the presence of different plume components characterized by an expansion dynamics occurring on different temporal scales. To recognize the spatial structure of the plume, on the right-hand part of each panel of figure 1, we also report the intensity versus z-distance plots, as obtained by integrating the emission along the x-axis. In particular, panel (*a*) indicates that at short time delays (<100 ns) both a fast, forward-directed component and a slow, long-lasting component are present.

The fast component is characterized by an intense emission core peaked at ≈ 1 mm from the target surface and a less intense shoulder extending from ≈ 2 to ≈ 6 mm along the normal to the target surface. Therefore, two different portions can be recognized in the fast component by the structure of the intensity versus z-distance plots of figure 1(*a*). The main fraction is composed of particles moving away from the target with an average velocity of $\approx 10\,\mathrm{km\,s^{-1}}$, while the smaller component is characterized by a velocity of $\approx 50\,\mathrm{km\,s^{-1}}$, along the normal to the target surface. At later times this fast plume gradually moves away from the target surface, while its overall emission drops rapidly in time and space.

In contrast, at this short time delay, a very slow component is still confined very close to the target surface (with spatial extension along the normal to the target surface of ≈ 0.2 mm), as observed in figure 1(*a*). The full dynamic expansion of this slow plume component, characterized by an expansion velocity of less than a few $\mathrm{km\,s^{-1}}$, takes place on a much longer timescale (several μs after the laser pulse arrival on the target surface), as shown in figure 1(*b*). This slow part of the ablated material remains close to the target surface up to very long time delays and is characterized by a quite different angular divergence with respect to the fast plume component. Moreover, its emission profile (right-hand-side of figure 1(*b*)) peaks at the target surface while gradually decreasing with z.

Spectrally resolved analysis of the plume emission has revealed that very different emission spectra characterize the two components. As an example, figure 2(*a*) shows a typical emission spectrum of the fast component, which is dominated by emission lines of the atoms of the target material. This
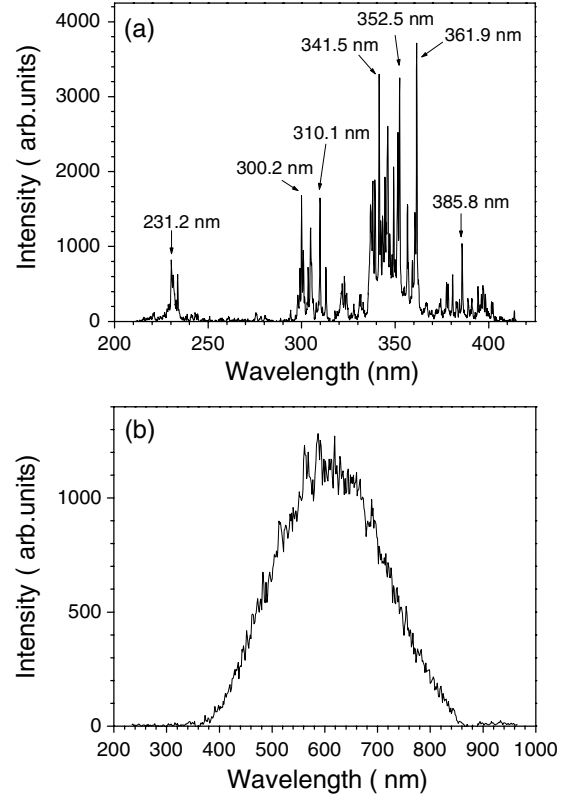
Figure 2. Typical emission spectra of the atomic (*a*) and nanoparticles (*b*) plume. The most intense Ni emission lines are indicated in panel (*a*).

allows us to identify the fast component as being due to atomic species of the target material. Instead, the slow plume typically shows a structureless, broadband continuum emission spectrum as reported in figure 2(*b*). This emission is characteristic of the radiative emission of small, nanometer-sized particles [2, 23]. We have obtained the size distributions of these particles by depositing the produced plume on mica substrates in high vacuum and at room temperature. Atomic force microscopy analysis of the deposits has shown that the slow component is mainly formed by Ni NPs whose radii range from a few nm to ≈ 50 nm, in our experimental conditions [11].

In figure 3 we report, as an example, a snapshot of the ablation plume obtained by the MD simulation at a time delay of 150 ps after the laser pulse onset, and at a laser fluence $F = 0.7\,\mathrm{J\,cm^{-2}}$. In spite of the rather short time delay, it is worth pointing out that this picture shows the main general features of the produced plume predicted by the MD simulations, since we have found that in the laser fluence range of concern to the present study, the general properties of plume expansion predicted by the model are already well established after just several tens of picoseconds. In particular, the simulations show that at this time the ablated material has already reached a free expansion regime, characterized by very few particle collisions, and the final ablation depth (≈ 100 nm in figure 3) has also been attained.

The MD simulations show that the top of the plume mainly consists of atoms, while the ablated material located near the metal surface, which is about 100 nm in depth at 150 ps after the laser pulse onset, is composed of clusters having sizes of up to
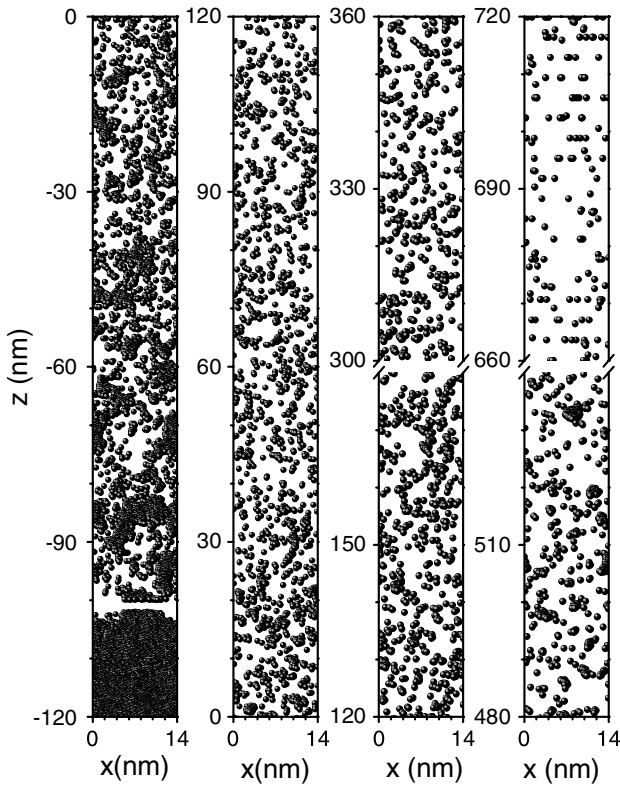
Figure 3. Snapshots of the MD simulations of the ablation process at 150 ps after the laser pulse onset at different positions. $F = 0.7\,\mathrm{J\,cm^{-2}}$; $\lambda = 527$ nm; $\tau_p = 300$ fs. In the figure $z = 0$ corresponds to the initial surface of the sample, while negative values of z correspond to the interior of the original target material.

about 15 nm. Due to the size limitation of the simulation cell, the absolute values of the nanoclusters sizes obtained in the MD simulations cannot be directly compared with those of the nanoparticles observed in the experiments. Nevertheless, the MD snapshots do substantiate very clearly the presence of nanoaggregates and the layered structure of the ablation plume. Thus, the structure and composition of the plume observed in figure 3 demonstrate a spatial segregation of the species produced during the laser ablation of metals which gives rise, on a longer timescale, to the experimental observation of a plume composed of two main components, atoms and NPs, characterized by different expansion dynamics and optical emission properties, as discussed above with reference to figures 1 and 2.

As a further confirmation of the above interpretation, we report in figure 4 the calculated density profile of the ablated material in the same conditions of figure 3, but on a longer spatial scale (up to 10 μm). The density profile of figure 4 indicates that a multi-component structure is already present in the nascent plume shortly after the laser pulse onset (e.g. 150 ps), with a two-cloud single-particle, atomic plume extending far above the original target surface, while the nanoclusters are still confined close to the target surface. These features are in rather good agreement with the plume structure evidenced by fast photography in figure 1, showing the presence of two different fractions in the spatial structure of the atomic plume component, followed by a cloud of NPs on a longer timescale. This also anticipates the significant
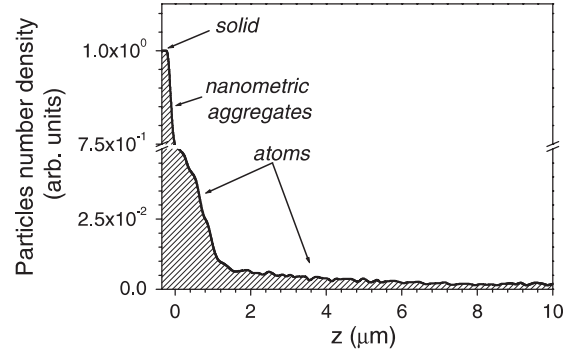
Figure 4. Number density of the ejected particles taken 150 ps after the laser pulse onset. $F = 0.7\,\mathrm{J\,cm^{-2}}$; $\lambda = 527$ nm; $\tau_p = 300$ fs. In the figure $z = 0$ corresponds to the initial surface of the sample, while negative values of z correspond to the interior of the original target material.
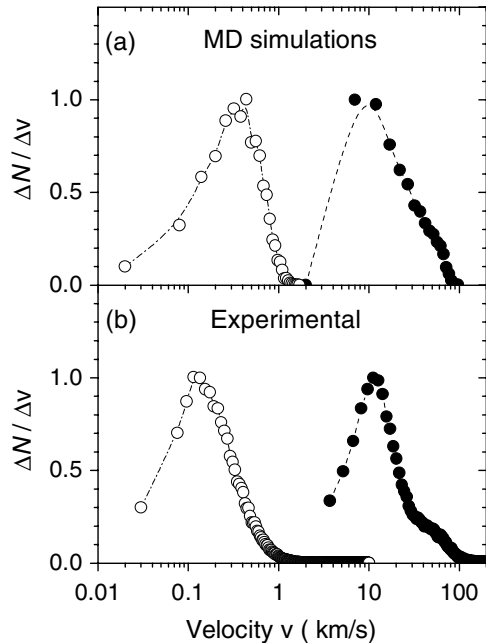
Figure 5. Velocity distributions of the ablated atoms ($\bullet$) and nanoparticles ($\circ$): (*a*) The MD simulation at a laser fluence $F = 0.7\,\mathrm{J\,cm^{-2}}$; (*b*) experimental results at a laser fluence $F \approx 0.8\,\mathrm{J\,cm^{-2}}$.

difference in the velocity expansion of the various species produced during the laser ablation with fs laser pulses, which is discussed below.

In figure 5, we report a comparison between the velocity distributions of the ablated species in the plume obtained by the MD simulations (see figure 5(*a*)), and the experimental distribution obtained from the optical characterization of the plume emission by time-gated imaging (see figure 5(*b*)), at laser fluences well above the ablation threshold. The experimental velocity distributions have been obtained by considering the spatial profiles of the plume along the normal to the target surface, at two different time delays. Each distribution in figure 5 has been normalized to its own maximum value to facilitate the comparison. A pretty good agreement between the numerical and the experimental velocity distribution can be observed in figure 5. The MD

simulations predict a most probable velocity of $\approx 10\,\mathrm{km\,s^{-1}}$ for the main, fast, atomic component, while the smaller component of even faster atoms, located ahead of the main plume as evidenced by the shoulder in the velocity distribution profile of figure 5(*a*), can reach velocities as high as $80\,\mathrm{km\,s^{-1}}$. On the other hand, the velocity distribution of the clusters predicted by the MD model are characterized by a most probable velocity of $\approx 0.3\,\mathrm{km\,s^{-1}}$, more than an order of magnitude lower than that of single, atomic particles. The experimental velocities distributions reported in figure 5(*b*) exhibit values of the velocity comparable with those predicted by the numerical model, both for the atomic and nanoparticles components, and a structure of the velocity profile surprisingly similar to the model predictions. In particular, for the atomic component both the most probable velocities ($\approx 10\,\mathrm{km\,s^{-1}}$) and the presence of a shoulder at higher velocities are rather well reproduced, while the experimental distribution is a bit narrower than the numerical one. As for the NPs component, the experimental most probable velocity is lower by a factor of ≈ 3 with respect to the numerical prediction, while the maximum velocity is fairly well reproduced. The discrepancies observed in the case of NPs may be ascribed to the size limitation of the MD simulation which results in smaller clusters with respect to those observed in the experiments [11], while the differences in the velocity distribution profiles may be due to the uniform spatial distribution of the laser intensity on the target surface used in the model. Nevertheless, the reliability of the comparison between the MD simulations results and the experimental findings provides a valuable confirmation of the view that the main features of the plume expansion in vacuum are established in the first stages (tens to hundreds of picoseconds) of its formation.

4.2. Plume components and nanoparticles formation

In this section, the mechanisms underlying the formation of the different species constituting the ablated plume are investigated by considering the temperature distribution produced by the laser pulse in the material, as well as the subsequent evolution of the different heated layers in a temperature–density ($T-\rho$) thermodynamic space.

Figure 6 reports the temperature distribution within the material obtained by the MD simulations at different times after the laser pulse onset. After 10 ps, which is the typical electron–lattice temperature equilibrium time in Ni, a surface layer of about 100 nm undergoes significant overheating. This layer, whose depth is mainly governed by the electron heat diffusion mechanism, is the one undergoing the ablation process, thus resulting in the plume shown in the snapshots of figure 3. As shown in figure 6, the material temperature reaches very large values, and it can even exceed the critical temperature ($T_c = 9470\,\mathrm{K}$) [7] in the uppermost layers (up to a distance from the initial surface of ≈ 30–$40\,\mathrm{nm}$). From figure 6 we can also observe that the temperature does not show a monotonous decrease with depth inside the sample ($z < 0$) but shows some wiggles as a consequence of changes in the local density induced by the thermal expansion and the propagation of stress wave in the material. Moreover, as a consequence of expansion and decomposition of the surface region the temperature of the
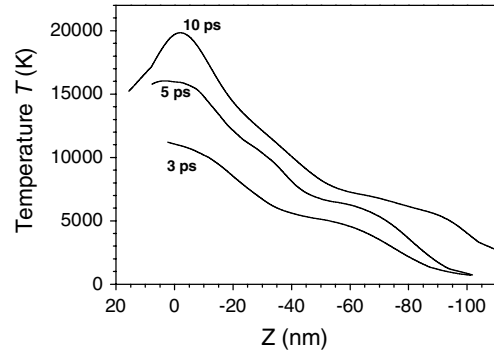
Figure 6. Temperature distribution in depth of the material at different moments after the laser pulse onset. $F = 0.7\,\mathrm{J\,cm^{-2}}$; $\lambda = 527\,\mathrm{nm}$; $\tau_p = 300\,\mathrm{fs}$. In the figure $z = 0$ corresponds to the initial surface of the sample, while negative values of z correspond to the interior of the original target material.
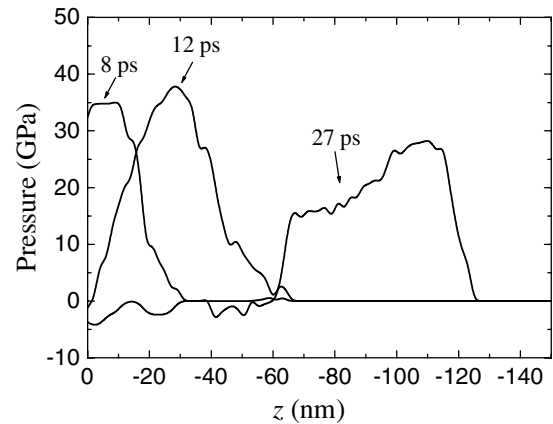
Figure 7. Pressure distribution in depth of the material at three different moments after the laser pulse onset. $F = 0.7\,\mathrm{J\,cm^{-2}}$; $\lambda = 527\,\mathrm{nm}$; $\tau_p = 300\,\mathrm{fs}$. In the figure, $z = 0$ corresponds to the initial surface of the sample.

expanding front ($z > 0$) becomes progressively lower than the interior temperature ($z < 0$). The fast heating of the surface region at nearly constant volume results in the development of a significant compression. Figure 7 represents the distribution of the pressure into the material at three subsequent moments after the laser pulse onset. As seen, a compression wave with a magnitude of about 40 GPa is developed during the heating of the lattice by the electron component. Then, this compression results in a fast expansion of the heated volume, leading to its phase transition and decomposition. It is worth mentioning that numerical simulations of the fs ablation process of Ni carried out in similar conditions by other groups (see, e.g. [7, 19]), showed a very similar behaviour of the thermodynamical parameters. Small quantitative differences can be related to the different material parameters used by the different groups.

In order to clarify the formation of different species into the ablated plume, the thermodynamic trajectories of different layers, located at different depths into the material, are traced in the temperature–density ($T-\rho$) space [7–9]. In figure 8 we report some typical $T-\rho$ trajectories for material volumes initially located at three different depths underneath the surface. The phase diagram for Ni is taken from [7], where the Morse potential is also used to describe the Ni system.
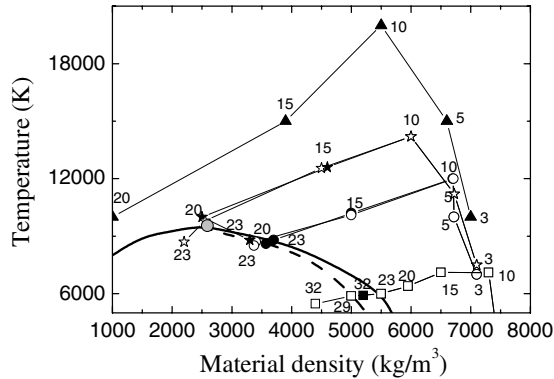
Figure 8. T–ρ trajectories for material volumes initially located at different depths beneath the material surface. $F = 0.7\,\mathrm{J\,cm^{-2}}$; $\lambda = 527\,\mathrm{nm}$; $\tau_p = 300\,\mathrm{fs}$. The phase diagram is taken from [7]. The thick solid and dashed curves represent the binodal and spinodal, respectively. The grey dot shows the critical point. The points labelled with triangles, stars, circles and squares represent the thermodynamic paths of the material initially located at depths of about 5, 20, 30 and 98 nm, respectively, in the sample. The solid and open symbols correspond to the material which is finally (at the end of the simulation time) in liquid or gas phase, respectively. The number adjacent to each point corresponds to the time after the laser pulse onset in ps.

The thick solid and dashed curves represent the binodal and spinodal. The grey dot marks the critical point. The numbers attached to each data point correspond to the time (in ps) elapsed from the laser pulse onset.

In figure 8, the solid triangles show the thermodynamic paths of the material initially located at depth of about 5 nm. During the relaxation, the corresponding T–ρ trajectory passes above the critical point, and the material is directly decomposed into the gas phase without an intermediate liquid–gas coexistence.

The stars in figure 8 show the trajectories for material initially located at depth of about 20 nm below the initial material surface. The solid and open stars correspond to the material which is in liquid and gas phase, respectively, at the end of the simulation. The temperature of the material at this depth reaches a value of about $1.5T_c$ during the time of energy transfer from the electron system to the lattice. The material undergoes fast expansion and about 7 ps later it starts to decompose. The trajectory of the material which is finally in the gas phase develops into the unstable zone in the direction of decreasing density (left from the critical point); meanwhile, the trajectory of the part of the material which is finally in the liquid phase proceeds through the increase in the density and out of the unstable zone. As in the present conditions the separation of the different phases is observed just before the material enters the unstable region, following [8] and [9], the matter removal mechanism can be attributed to a *fragmentation* process in which the material undergoes decomposition leading to a heterogeneous, clustered phase as a consequence of the rapid expansion of a supercritical fluid.

The circles in figure 8 show the T–ρ trajectories for the material initially located 30 nm below the metal surface. Again, the solid and open circle represent the material which is in the liquid or gas phase at the end of the simulation. In this case the matter is heated to about $1.2\ T_c$, and after

Table 1. Values of the ablation depth d obtained in micro-hole drilling experiments (Exp.), and predicted by the molecular dynamics simulations (MD).

	Ablation depth d (nm)	
F (J cm^{-2})	MD	Exp.
0.04	—	0
0.10	9.5	5
0.20	24.6	—
0.30	34.5	28
0.40	44.2	50
0.80	—	100

a fast expansion the material enters the metastable region located between the binodal and spinodal lines. Approaching the spinodal, the gas phase starts to nucleate, a mechanism described as *phase explosion* in the literature [7–9]. Our analysis shows that the mechanism of phase explosion is responsible for the decomposition of the material initially located at a depth of about 100 nm below the initial material surface. Typical thermodynamic trajectories for the liquid and gas phases of the material at this depth are presented in figure 8 as solid and open squares, respectively. At the end of the simulation, the material initially located deeper than ≈100 nm is in a dense state and we do not observe any decomposition (gas phase or spallation) of this part during the evolution of the system.

The difference in the structure of the ablated material along the z axis can be attributed to the different degree of material heating introduced by the free electrons heat conduction that redistributes the absorbed laser energy. The absorbed energy is actually spread into a depth of the material which is about an order of magnitude larger than the optical skin depth ($\ell_{opt} \approx 13.4$ nm). As a result, while this energy redistribution decreases the temperature gradient, different layers beneath the original surface of the material reach rather different temperatures. This results in the realization of the conditions leading to the different decomposition mechanisms. The material located initially (at the beginning of the ablation process) at the surface is heated far above the critical temperature and direct decomposition into the gas phase is realized. More deeply into the target, the thermodynamic conditions achieved after ultrashort laser pulse heating lead to a material decomposition which is largely dominated by the mechanism of phase explosion. Thus, the transition from overheated liquid to the liquid–gas phase is the primary mechanism for the formation of the nanoparticles observed into the ablation plume.

4.3. Fluence dependence of the ablation yield

A point of specific interest in the characterization of the laser ablation process is the variation of the ablation yield with the laser fluence. In table 1 we report a direct comparison between ablation depth obtained in micro-hole drilling experiments and the values predicted by the MD simulations. The calculated ablation depth follows the same dependence of the experimental data, indicating a good consistency between the prediction of the MD simulations and the experimentally observed behaviour. In particular, the model is able to
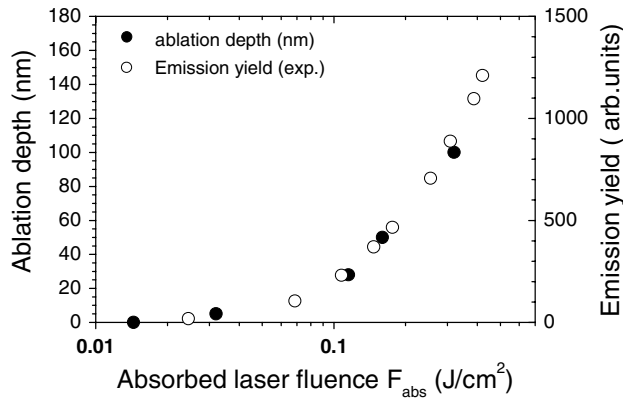
Figure 9. Ablation depth (●) and plume emission yield (○) ablation depth as function of the absorbed laser fluence.

reproduce the main characteristic of the experimental data, namely, the strongly nonlinear behaviour.

In figure 9 we report the dependence on the absorbed laser fluence of the ablation depth (solid dots), obtained in micro-hole drilling experiments, and of the optical emission yield (open dots) of the plume. The absorbed laser fluence $F_{abs} = (1 - R)F$ is used in order to compare the experimental data corresponding to different angles of incidence of the laser radiation on the sample surface. The optical emission yield of the plume has been obtained by integrating the overall optical emission signal from the expanding ablation plume [24]. In figure 9 two different regimes of ablation can be observed: an almost logarithmic dependence from the threshold up to $F_{abs} \approx 0.16\,\text{J\,cm}^{-2}$ ($F \approx 0.4\,\text{J\,cm}^{-2}$) is progressively followed by a steeper increase at larger fluences, above $F_{abs} \approx 0.2\,\text{J\,cm}^{-2}$ ($F \approx 0.5\,\text{J\,cm}^{-2}$). By extrapolating to zero the observed dependence in the low-fluence regime, we estimate a fluence threshold of $F_{abs} \approx 0.02\,\text{J\,cm}^{-2}$ ($F \approx 0.05\,\text{J\,cm}^{-2}$) for nickel ablated by $\approx 300\,\text{fs}$ laser pulses at 527 nm at normal incidence. The experimental emission yield shows a dependence on the absorbed laser fluence very similar to the ablation depth, with a threshold in satisfactory agreement with both the experimental ablation depth and the theoretical estimate. This is a rather interesting result, since it indicates that also in the case of ultrashort laser ablation of matter the overall amount of radiation emitted by the expanding plume turns out to be reasonably proportional to the amount of ablated material. Thus, also in this case plasma radiation monitoring can be safely used to characterize the ablation process.

To conclude the characterization of the ultrashort laser ablation process, we discuss how the numerical model provides a simple physical interpretation of the observed nonlinear dependence of the ablation depth on laser fluence. In figure 10(a) the dependence of the experimental ablation depth, d, is compared with the variation of the electron heat diffusion length, l_e (solid line) with the laser fluence. In figure 10(b) the values of d and l_e are also plotted against each other to show the correlation between the two variables. The electron heat diffusion depth is estimated as the maximal depth where the electron temperature $T_e \neq 300\,\text{K}$ for the characteristic time of the electron–lattice equilibration. The latter is estimated from the moment where $T_i = T_e$ on the material surface. These parameters are obtained on the basis of the two-temperature
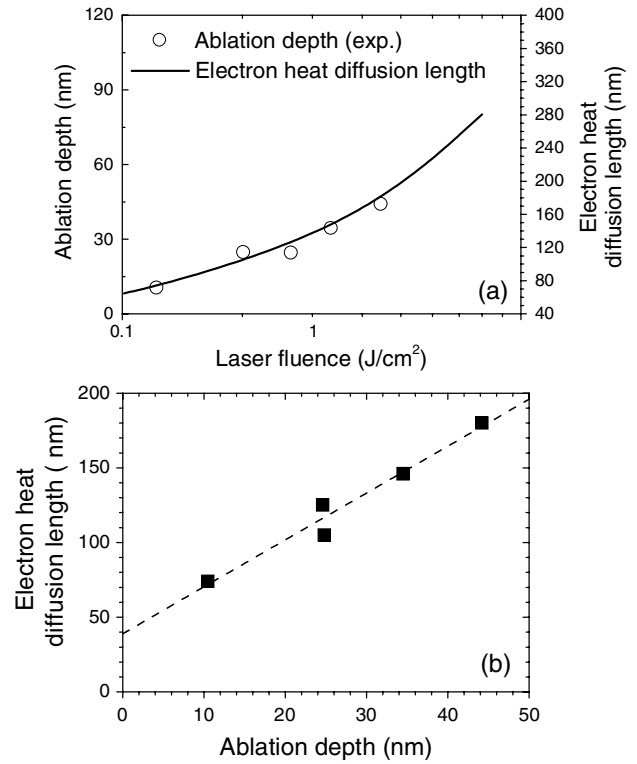
Figure 10. (*a*) Comparison between the dependences of the measured ablation depth (○) and the electron heat diffusion length (solid line) on the absorbed laser fluence, in the range 0.1–1 J cm^{-2}; (*b*) electron heat diffusion length versus ablation depth. See text for details.

diffusion model. We point out that the units of the vertical axes of figure 10(a) have been suitably rescaled to allow a direct comparison of the laser pulse fluence dependences of the experimental ablation depth and of the calculated electron heat diffusion length. In the fluence range of concern here (see figure 10(a)), the electron heat diffusion length results always larger than the material skin depth ($\approx 13\,\text{nm}$). As seen, the agreement between the dependences on laser fluence of the two variables is fairly good, and one can, thus, conclude that the two different regimes of ablation characterizing the process at low (below $F_{abs} \approx 0.16\,\text{J\,cm}^{-2}$) and relatively high fluences are strictly related to the contribution of the electron heat diffusion in the process of redistribution of the absorbed energy. Finally, from figure 10(b) we can observe that above the ablation threshold the electron heat diffusion length is roughly three times the experimental ablation depth, over the investigated laser fluence range. Besides, extrapolation of the heat diffusion length at $d = 0$ seems to suggest that when the laser ablation threshold is reached the laser energy has diffused over a length of $\approx 40\,\text{nm}$ inside the sample, i.e. about three times the laser optical penetration depth ℓ_{opt}.

5. Conclusions

The present experimental and numerical analysis of the femtosecond laser ablation of a nickel target provides a coherent physical picture of ultrashort laser ablation of the metal targets in vacuum, that can also be extended to other solid targets, Si e.g. as briefly discussed below.

In this study we have used $\approx$300 fs visible (527 nm) laser pulses in a fluence range from the ablation threshold for Ni ($\approx$0.05 J cm^{-2}) up to $\approx$1 J cm^{-2}, and the experimental characterization of the ablation process has been carried out by two different, complementary approaches: (i) analysis of the properties of the material blow-off during its vacuum expansion by using fast photography and optical emission spectroscopy; (ii) study of the dependence of ablation depth on laser fluence by means of SEM analysis of micro-holes drilled into the metallic samples. In parallel, ultrashort laser heating of the material and its subsequent relaxation has been modelled theoretically by using MD simulations coupled to the two-temperature model, thus providing a means for supporting and interpreting the characteristic experimental features of the process.

Both the experimental analysis and the theoretical predictions evidence the two main features of the process: (i) the splitting of the ejected plume into two main components, namely, a fast atomic component, characterized by a rather high vacuum expansion velocity (of the order of a few tens of km s^{-1}), preceding a very slow cloud of ejected material with an expansion velocity more than ten times smaller than that of the atomic component; (ii) the fact that the second, slow plume component is mainly composed of Ni nanoparticles with sizes ranging from a few nm to tens of nm.

The origin of the spatial and energetic segregation of the two classes of species observed in the plume, as well as of their specific composition, has been identified by tracing the relaxation paths of the irradiated matter in the temperature–density diagram of the material. The temperature state at which the layers located at different depths into the materials are forced by the extreme heating induced by the ultrashort laser pulse irradiation results in the simultaneous occurrence of various decomposition mechanisms. The uppermost surface layers are overheated and directly decomposed into the gas phase leading to the generation of the fast atomic component, meanwhile decomposition of the material located more deeply into the solid target mainly occurs through a phase explosion mechanism. This, in turn, results in the direct production of the nanoparticles observed in the plume.

Another point of relevant interest of the process is the dependence of the ablation depth and of the overall plume optical emission yield on laser fluence. The experimentally observed values have been compared with the ablation rate obtained by the numerical model, resulting in fairly good agreement. This comparison clearly demonstrates that the observed nonlinear dependence of the ablation yield on laser fluence is related to the variation of the electron heat diffusion length with the temperature, and hence with laser fluence, occurring during the process of redistribution of the absorbed energy.

As a final remark, we emphasize that although the present study has been carried out in the specific case of nickel, the main experimental features we have observed are characteristics of the plume produced by irradiation of all the metals, as well as of other significant materials, e.g. silicon, with ultrashort laser pulses with durations in the range 100 fs–1 ps, and at intensities above the ablation threshold [2, 4, 11]. This allows us to draw the conclusion that for laser pulses whose duration is both much longer than the energy thermalization time of the hot electron bath generated by the absorption of laser radiation in the target ($\approx$ few tens of fs), and sufficiently shorter than the electrons–lattice energy relaxation time (typically several ps), the material evolution and quenching which follows the extreme conditions of the temperature and the pressure induced in the target take place essentially in a similar way. Therefore, the numerical analysis of ultrashort laser ablation of solid targets of the present paper can be safely assumed to essentially retain its validity in the whole temporal range of $\approx$100 fs–1 ps. Our results confirm and extend those very recently published in the literature by different groups [1–5, 7–11, 25], supporting the idea that different materials behave roughly the same when irradiated by ultrashort pulses at intensities above the threshold for ablation. In these conditions, the very general mechanisms responsible for the ejection of matter always seem to lead to similar, characteristic features, regardless of the specific nature of the target material. Finally, our analysis confirms that laser ablation carried out in the above conditions inevitably leads to the generation of nanoparticles of the target material, a characteristic of prominent interest in the basic field of nanophysics, and also in view of possible technological applications for nanodevices.

Acknowledgments

References

[1] Albert O, Roger S, Glinec Y, Loulergue J C, Etchepare J, Boulmer-Leborgne C, Perriere J and Millon E 2003 *Appl. Phys.* A **76** 319
[2] Amoruso S, Bruzzese R, Spinelli N, Velotta R, Vitiello M, Wang X, Ausanio G, Iannotti V and Lanotte L 2004 *Appl. Phys. Lett.* **84** 4502
[3] Eliezer S *et al* 2004 *Phys. Rev.* B **69** 144119
[4] Amoruso S, Ausanio G, Bruzzese R, Vitiello M and Wang X 2005 *Phys. Rev.* B **71** 033406
[5] Ausanio G, Barone A C, Iannotti V, Lanotte L, Amoruso S, Bruzzese R and Vitiello M 2004 *Appl. Phys. Lett.* **85** 4103
[6] Anisimov S I, Kapelovich B L and Perel'man T L 1974 *Zh. Eksp. Teor. Fiz.* **66** 776
[7] Cheng Ch and Xu X 2005 *Phys. Rev.* B **72** 165415
[8] Perez D and Lewis L J 2003 *Phys. Rev.* B **67** 184102
[9] Lorazo P, Lewis L J and Meunier M 2006 *Phys. Rev.* B **73** 134108
[10] Nedialkov N N, Imamova S E and Atanasov P A 2004 *J. Phys. D: Appl. Phys.* **37** 638
[11] Amoruso S, Ausanio G, Barone A C, Bruzzese R, Gragnaniello L, Vitiello M and Wang X 2005 *J. Phys. B: At. Mol. Opt. Phys.* **38** L329
[12] Allen M P and Tildesley D J 1987 *Computer Simulation of Liquids* (Oxford: Clarendon)
[13] Girifalco L A and Weizer V G 1959 *Phys. Rev.* **114** 687
[14] Sutton A P and Ghen H 1990 *J. Phil. Mag. Lett.* **61** 139
      Zhao J, Wang S Q, Yang Z Q and Ye H Q 2001 *J. Phys.* **13** 8061

[15] Liu W K, Yuan J M and Lin S H 1999 *Phys. Rev.* A **60** 1363
[16] Imamova S E, Atanasov PA and Nedialkov N N 2005 *Nucl. Instrum. Methods. Phys. Res.* B **227** 490
[17] Zhigilei L V and Garrison B J 1999 *Mater. Res. Soc. Symp. Proc.* **538** 491
[18] Lynch D W and Hunter W R 1985 *Handbook of Optical Constants of Solids* ed E D Palik (New York: Academic)
[19] Zhigilei L V and Ivanov D S 2005 *Appl. Surf. Sci.* **248** 433
[20] Chen J K, Beraun J E and Tham C L 2002 *J. Opt.* A **4** 650
[21] Aschcroft N W and Mermin N D 1976 *Solid State Physics* (New York: Holt, Rinehart and Winston)
[22] Press W H, Teukolsky S A, Vetterling W T and Flannery B P 1992 *Numerical recipes in Fortran* vol 1 (Cambridge: Cambridge University Press)
[23] Amoruso S, Bruzzese R, Spinelli N, Velotta R, Vitiello M and Wang X 2004 *Europhys. Lett.* **67** 404
[24] Pronko P P, VanRompay P A, Horvath C, Loesel F, Juhasz T, Liu X and Mourou G 1998 *Phys. Rev.* B **58** 2387
[25] Amoruso S, Bruzzese R, Vitiello M, Nedialkov N N and Atanasov P A 2005 *J. Appl. Phys.* **98** 044907